



CHORUS

This is the accepted manuscript made available via CHORUS. The article has been published as:

Realization of interlayer ferromagnetic interaction in $\text{MnSb}_{\{2\}}\text{Te}_{\{4\}}$ toward the magnetic Weyl semimetal state

Taito Murakami, Yusuke Nambu, Takashi Koretsune, Gu Xiangyu, Takafumi Yamamoto, Craig M. Brown, and Hiroshi Kageyama

Phys. Rev. B **100**, 195103 — Published 4 November 2019

DOI: [10.1103/PhysRevB.100.195103](https://doi.org/10.1103/PhysRevB.100.195103)

Realization of interlayer ferromagnetic interaction in MnSb₂Te₄ toward the magnetic Weyl semimetal state

Taito Murakami¹, Yusuke Nambu², Takashi Koretsune³, Gu Xiangyu¹, Takafumi Yamamoto¹, Craig M. Brown⁴, and Hiroshi Kageyama^{1,5*}

¹ Department of Energy and Hydrocarbon Chemistry, Graduate School of Engineering, Kyoto University, Nishikyo-ku, Kyoto 615-8510, Japan

² Institute for Materials Research, Tohoku University, Sendai, Miyagi 980-8577, Japan

³ Department of Physics, Tohoku University, Sendai, Miyagi 980-8578, Japan

⁴ Center for Neutron Research, National Institute of Standards and Technology, Gaithersburg, MD20899, USA

⁵ CREST, Japan Science and Technology Agency (JST), Kawaguchi, Saitama 332-0012, Japan

ABSTRACT

Magnetic properties of MnSb_2Te_4 were examined through magnetic susceptibility, specific heat, and neutron diffraction measurements. As opposed to isostructural MnBi_2Te_4 with the antiferromagnetic ground state, MnSb_2Te_4 develops a spontaneous magnetization below 25 K. Our first principle calculations on the material in a ferromagnetic state could be interpreted as a type-II Weyl semimetal state with broken time-reversal symmetry. Detailed structural refinements using x-ray diffraction and neutron diffraction data reveal the presence of site-mixing between Mn and Sb sites, leading to the ferrimagnetic ground state. With theoretical calculations, we found that the presence of site-mixing plays an important role for the interlayer Mn-Mn ferromagnetic interactions.

INTRODUCTION

Topological semimetals (TSMs), characterized by crossings of valence and conduction bands in the momentum space, have brought exciting opportunities to explore properties that are unattainable in conventional semimetals or metals [1–5]. Dirac semimetal is the first experimentally confirmed TSMs, where a fourfold degenerate Fermi point is topologically protected by time-reversal symmetry (TRS) as well as space-inversion symmetry (SIS). This type of materials has been experimentally verified in systems including Cd_3As_2 and Na_3Bi [6–9]. The degeneracy at the Dirac point can be lifted by breaking of either symmetry, leading to the Weyl semimetal state. The resultant twofold degenerated Weyl points have a distinct chirality, resulting in an open arc surface state and chiral anomaly at high magnetic fields [9–11]. Weyl semimetals have been found in materials without SIS (e.g., NbP and TaAs) [12–14] or TRS (e.g., Mn_3Sn and $\text{Co}_3\text{Sn}_2\text{S}_2$) [15,16].

A new class of TSMs called “Type-II TSMs” has recently been proposed from theoretical perspectives [17]. Unlike conventional type-I TSMs, Dirac cones in type-II TSMs are largely tilted along certain momentum directions, violating the Lorentz invariance [17]. The distinct band topology leads to extremely anisotropic magnetoresistance [17,18]. After the prediction of type-II Weyl semimetal state in WTe_2 , several compounds were shown as type-II Weyl semimetal without SIS, including MoTe_2 , LaAlGe , and TaIrTe_4 [19–25]. On the other hand, the experimental study of TRS-broken type-II Weyl semimetal is rather scarce. A rare example is the layered bismuthide YbMnBi_2 , where the canting of Yb moment from the c axis was initially proposed to break the TRS, resulting in the type-II Weyl semimetal state [26]. Subsequent optical conductivity measurements in YbMnBi_2 however failed to confirm the canted Yb moments [27]. More recently, LnAlGe ($\text{Ln} = \text{Ce}, \text{Pr}$) have been predicted as a TRS broken TSM with both type-I and type-II crossings [28].

Ternary tellurides MPn_2Te_4 ($M = \text{Ge}, \text{Sn}, \text{Pb}, \text{Mn}$ and $\text{Pn} = \text{As}, \text{Sb}, \text{Bi}$) have a layered structure as shown in Fig. 1(a) [29–31]. MnBi_2Te_4 with magnetic ions was theoretically proposed to have an antiferromagnetic topological insulating state [32–36], which was later confirmed from experimental studies [35–37]. It was also predicted that this material becomes TRS broken type-II Weyl semimetal if Mn moments are aligned ferromagnetically [34], a situation that has not been observed experimentally. In this study, we newly synthesized isostructural MnSb_2Te_4 and conducted magnetic susceptibility, specific heat, and neutron diffraction measurements. Unlike the previous theory on MnSb_2Te_4 showing the A-type antiferromagnetic state [38], a ferromagnetic component develops in MnSb_2Te_4 below 25 K. Density functional theory (DFT) calculations suggest that MnSb_2Te_4 in a ferromagnetic state can be expected to be a TRS broken type-II Weyl semimetal. Structural refinements using x-ray diffraction (XRD) and neutron diffraction data, however, reveal the presence of site-mixing between Mn and Sb sites, leading to the ferrimagnetic ground state. The effect of site-mixing is investigated through first principle calculations.

EXPERIMENTAL AND CALCULATION DETAILS

A polycrystalline sample of MnSb_2Te_4 was synthesized via the solid-state reaction. Mn, Sb, and Te (99.99%, Kojundo Chemical) were weighed in a stoichiometric ratio, mixed and pelletized in a nitrogen filled dry box. A pellet was sealed in an evacuated silica tube and heated up to 600 °C and kept for 10 hrs. Powder X-ray diffraction (PXRD) experiments were performed using Bruker AXS D8 ADVANCE with $\text{Cu-K}\alpha$ radiation.

DC magnetic susceptibility was measured by a commercial SQUID magnetometer (Quantum Design, MPMS) in the temperature range of 2–350 K under the magnetic field of 0–7 T. Specific heat C_{total} was measured by the relaxation method using a physical property measurement system (Quantum Design, PPMS) down to 2 K. To estimate the lattice contribution C_{L} , we obtained the thermal variation of the Debye temperature $\theta_{\text{D}}(T)$ for the isostructural nonmagnetic analogue GeSb_2Te_4 using the Debye equation. $\theta_{\text{D}}(T)$ of MnSb_2Te_4 was then estimated by multiplying a scaling factor according to $\theta_{\text{D}} \propto M_0^{-1/2} V_0^{-1/3}$, where M_0 and V_0 are molar ratio mass and volume, respectively. C_{L} was obtained by converting the scaled $\theta_{\text{D}}(T)$ into specific heat. Detail of the analysis is provided in the Supplemental Material [39]. Electronic structure calculations were performed within the generalized gradient approximation using the Vienna *ab initio* simulation package (VASP) [40,41].

Powder neutron diffraction (PND) data were collected at 50 K and 5 K using the high-resolution powder diffractometer BT-1 ($\lambda = 2.08 \text{ \AA}$) at the NIST Center for Neutron Research, USA. The obtained diffraction data were structurally refined using the JANA2006 [42] and FullProf Suite [43]. We employed group theoretical analysis to identify magnetic structures that are allowed by symmetry.

RESULTS AND DISCUSSIONS

Figure 1(b) shows the room-temperature XRD profile of the target compound. All the observed Bragg peaks can be indexed based on the rhombohedral unit cell. The lattice parameters of $a = 4.2385(3) \text{ \AA}$ and $c = 40.8497(3) \text{ \AA}$ are slightly smaller than those of MnBi_2Te_4 ($a = 4.334 \text{ \AA}$ and $c = 40.910 \text{ \AA}$) [31], which is reasonable given the smaller ionic radius of Sb than that of Bi. Figure 1(a) displays the structure of MnSb_2Te_4 (space group $R\bar{3}m$), with NaCl-type MnTe layers and tetradymite-type Sb_2Te_3 layers stacking alternatively along the c axis. The edge-shared MnTe_6 octahedral layer forms a regular triangular lattice. Since the formal valence is given by $(\text{Mn}^{2+})(\text{Sb}^{3+})_2(\text{Te}^{2-})_4$ and Mn^{2+} in a high spin configuration has quenched orbital degree of freedom, one can expect Heisenberg-type magnetic behavior in this material.

S. V. Eremeev *et al.* predicted that MnSb_2Te_4 has the A-type antiferromagnetic ground state, where the ferromagnetic Mn layers are stacked antiferromagnetically [38]. However, as shown in Fig. 2(a), the magnetic susceptibility of MnSb_2Te_4 in an applied field of 0.1 T rapidly increases below around 30 K, suggesting a transition to a ferromagnetic state (which, however, will be corrected

later). From the Arrott plot (Fig. 2(c)), the transition temperature, T_C , is estimated to be 25 K, close to the Néel temperature of 24.2 K observed in MnBi_2Te_4 [35–37,44]. The isotherm magnetization curve at 5 K up to 7 T (Fig. 2(b)) shows a small but finite ferromagnetic hysteresis loop. Such a small hysteresis has been sometimes reported in ferro- or ferri-magnets such as yttrium iron garnet [45]. The Curie-Weiss fitting yields the effective magnetic moment of $\mu_{\text{eff}} = 5.842(7) \mu_B$, in good accordance with the value expected from the high-spin state of Mn^{2+} ($5.92 \mu_B$). Figure S1 in the Supplemental Material shows a difference in neutron data between $T = 5$ K and 50 K. This clearly shows the increase of several nuclear reflections (e.g., 101 and 104) below T_C , which is consistent with the ferromagnetic order with the magnetic wave vector $\mathbf{q}_m = (0, 0, 0)$.

The magnetic transition is further probed by heat capacity experiments. As shown in Figure 3(a), the total specific heat C_{total} below 30 K is noticeably larger than that of the isostructural nonmagnetic GeSb_2Te_4 , indicating the magnetic contribution to the specific heat. Its magnetic component C_{mag} is estimated by subtracting the lattice contribution from the data using GeSb_2Te_4 (Fig. 3(b), left axis). Magnetic entropy, S_{mag} , calculated from the integration of C_{mag}/T (Fig. 3(b), right axis), shows saturating behavior toward 30 K, followed by a gradual increase upon further warming. S_{mag} reaches about 11 J/mol K^2 at 100 K, slightly smaller than the expected value of $R \ln 6$ for $S = 5/2$, where R is the gas constant. This observation implies that the short-range correlation persists well above T_C . A power law behavior in $C_{\text{mag}} \propto T^\alpha$ with $\alpha = 1.52(1)$ is observed at temperatures below 10 K (Fig. 3(c)). If there is a long-range magnetic order, α follows the relation of $\alpha = d/\nu$, where d is the dimensionality of the magnon excitation and ν is related to the type of the magnetic order ($\nu = 1$ and 2 , respectively, stand for antiferromagnetic and ferromagnetic order). The observed $T^{3/2}$ dependence in MnSb_2Te_4 implies three-dimensional-like magnon excitations from a ferromagnetic state. However, the limited fitting range prevented us from further elucidation of the magnetic excitations.

As shown above, MnSb_2Te_4 undergoes a magnetic transition with a spontaneous magnetization, in contrast to the antiferromagnetic structure in MnBi_2Te_4 [36,37,44,46]. To obtain more insight into the ground state in MnSb_2Te_4 , we performed first principle calculations assuming a ferromagnetic state with an out-of-plane easy axis. Without the spin-orbit couplings (SOC), MnSb_2Te_4 is a semiconductor with a direct band gap of $E_g \sim 0.09 \text{ eV}$ (Fig. 4(a)). When SOC is turned on (Fig. 4(b)), we found for the first time a clear band inversion around the Γ point, forming a pair of band crossing along the Γ -Z line. The resultant Weyl cones are tilted with respect to the Γ -Z line, a characteristic feature of type-II Weyl points. From the observed spontaneous magnetization, we deduce that MnSb_2Te_4 is a potential TRS broken type-II Weyl semimetal at zero magnetic field.

It is noticed, however, that without SOC the antiferromagnetic (A-type) structure is more stable than the ferromagnetic one by 18.3 meV, similarly to the previous result [38], and inclusion of SOC hardly affects the relative energy difference (17.5 meV). The discrepancy from the ferromagnetic ground state is also inferred from the Curie-Weiss fitting for the susceptibility that yielded a negative

Weiss temperature of $\Theta_W = -21.6(4)$ K (Fig. 2(a)). Furthermore, the saturation magnetization of about $1.8 \mu_B/\text{Mn}$ at 5 K is somewhat smaller than that expected from high-spin Mn^{2+} .

These contradictory observations led us to investigate the structural details of MnSb_2Te_4 . A structural refinement was initially carried out assuming the ideal MnBi_2Te_4 -type structure ($R\bar{3}m$), which however resulted in rather poor reliability factors (e.g., $R_{\text{wp}} \sim 11\%$) (Fig. S2). Thus, site-mixing among cations was considered in the analysis by allowing Sb ($6c$) to occupy Mn ($3a$) site and vice versa, while the total occupancy factors were constrained to unity. This substantially improved the fitting (GOF = 1.77, $R_{\text{wp}} = 4.51\%$, and $R_p = 1.77\%$) and gave the chemical composition of $(\text{Mn}_{0.66}\text{Sb}_{0.34})(\text{Sb}_{0.83}\text{Mn}_{0.17})_2\text{Te}_4$. No site deficiency was found for the anionic sites. The full structural parameters are shown in Table I. Cation anti-site disorder also occurs in other MPn_2Te_4 -type compounds with a site-mixing ranging from 15% to 35% [47,48].

We refined the PND data to clarify the effect of site-mixing on the magnetism. Above T_C (at 50 K), the refined crystal structure is fully consistent with that obtained from the room-temperature XRD (Table I). At 5 K, we considered various magnetic structures including the ferromagnetic structure to account for the increased nuclear reflections. The best result with $R_{\text{wp}} = 8.38\%$ (Fig. 5(a)) was obtained for the ferrimagnetic structure, where the inter-exchanged Mn atoms at the $6c$ site align anti-parallelly along the c axis with respect to Mn atoms at the *original* $3a$ site. Magnetic moments are $4.3(2) \mu_B$ and $3.1(3) \mu_B$ for $3a$ and $6c$ sites, respectively. The sublattice magnetic moment of Mn is $2.1 \mu_B$ per unit cell, which is indeed in good accordance with the saturation magnetization value at 5 K (Fig. 2(b)).

The effect of site-mixing between Mn and Sb sites was considered for theoretical calculations (see Fig. S3 in the Supplemental Material). Here, we used two site-mixing patterns with a $\sqrt{3} \times \sqrt{3} \times 1$ supercell and calculated the ferromagnetic, ferrimagnetic and antiferromagnetic spin configurations along the $[001]$ direction. In all the cases, we found magnetic moments only at the Mn atoms. The calculated relative energies are summarized in Table S1 in the Supplemental Material. In the antiferromagnetic case, there are two choices for the magnetic moment of Mn atoms in the Sb layer so we considered their average. As opposed to the disorder-free configuration as described above, the ferrimagnetic structure was found to be most stable. This indicates that the site mixing alters the interlayer exchange coupling from antiferromagnetic to ferromagnetic. We note that the band structures of the ferrimagnetic structures have a band gap. Since these band structures highly depend on the site-mixing patterns, we speculate that a fully random anti-site mixing if achieved will recover the original crystal structure symmetry and the Weyl-semimetal phase may appear.

CONCLUSION

To summarize, we have synthesized a layered chalcogenide MnSb_2Te_4 and measured its fundamental physical properties. The observed spontaneous magnetization below 25 K, differing

from the antiferromagnetic order in MnBi_2Te_4 , can be explained in terms of the ferrimagnetic order where the inter-exchanged Mn moments are antiparallely coupled with the original Mn moments. First principle calculations show that the introduction of anti-site disorder plays a key role for the ferromagnetic interaction between Mn layers, which we believe an important step toward the TRS broken type-II Weyl semimetal state. It should be noted that the Sb sample used here is in a polycrystalline form, which may hamper the observation of the expected topological properties. For further analyses of the topological state in MnSb_2Te_4 , growth of single crystal is required, which is in progress. The known $MPn_2\text{Te}_4$ compounds have been predicted to have topological states including topological insulator, antiferromagnetic topological insulator, and topological axion state [35–37]. We demonstrate here that MnSb_2Te_4 represents the first example in this family possessing the interlayer ferromagnetic interaction, which warrants further development of topological physics.

ACKNOWLEDGMENT

This work was supported by CREST project and Grant-in-Aid for Scientific Research on Innovative Areas “Mixed anion” (16H6439, 16H6440, 17H05473, 19H04683), and Grant-in-Aid for Scientific Research (16H04007, 17H06137) from MEXT. T.M. was supported by JSPS for Young Scientists.

REFERENCES

- [1] H. Weng, X. Dai, and Z. Fang, *J. Phys. Condens. Matter* **28**, 303001 (2016).
- [2] B. Yan and C. Felser, *Annu. Rev. Condens. Matter Phys.* **8**, 337 (2016).
- [3] L. M. Schoop, F. Pielhofer, and B. V. Lotsch, *Chem. Mater.* **30**, 3155 (2018).
- [4] N. P. Armitage, E. J. Mele, and A. Vishwanath, *Rev. Mod. Phys.* **90**, 15001 (2018).
- [5] A. Bernevig, H. Weng, Z. Fang, and X. Dai, *J. Phys. Soc. Japan* **87**, 041001 (2018).
- [6] Z. K. Liu, B. Zhou, Y. Zhang, Z. J. Wang, H. M. Weng, D. Prabhakaran, S. Mo, Z. X. Shen, Z. Fang, X. Dai, Z. Hussain, and Y. L. Chen, *Science* (80-.). **343**, 864 (2014).
- [7] S. Borisenko, Q. Gibson, D. Evtushinsky, V. Zabolotnyy, B. Büchner, and R. J. Cava, *Phys. Rev. Lett.* **113**, 027603 (2014).
- [8] S. Jeon, B. B. Zhou, A. Gyenis, B. E. Feldman, I. Kimchi, A. C. Potter, Q. D. Gibson, R. J. Cava, A. Vishwanath, and A. Yazdani, *Nat. Mater.* **13**, 851 (2014).
- [9] J. Xiong, S. K. Kushwaha, T. Liang, J. W. Krizan, M. Hirschberger, W. Wang, R. J. Cava, and N. P. Ong, *Science* (80-.). **350**, 1314 (2015).
- [10] X. Huang, L. Zhao, Y. Long, P. Wang, D. Chen, Z. Yang, H. Liang, M. Xue, H. Weng, Z. Fang, X. Dai, and G. Chen, *Phys. Rev. X* **5**, 031023 (2015).
- [11] S. A. Parameswaran, T. Grover, D. A. Abanin, D. A. Pesin, and A. Vishwanath, *Phys. Rev. X* **4**, 031035 (2014).
- [12] L. X. Yang, Z. K. Liu, Y. Sun, H. Peng, H. F. Yang, T. Zhang, B. Zhou, Y. Zhang, Y. F. Guo, M.

- Rahn, D. Prabhakaran, Z. Hussain, S. K. Mo, C. Felser, B. Yan, and Y. L. Chen, *Nat. Phys.* **11**, 728 (2015).
- [13] C. Shekhar, A. K. Nayak, Y. Sun, M. Schmidt, M. Nicklas, I. Leermakers, U. Zeitler, Y. Skourski, J. Wosnitza, Z. Liu, Y. Chen, W. Schnelle, H. Borrmann, Y. Grin, C. Felser, and B. Yan, *Nat. Phys.* **11**, 645 (2015).
- [14] Z. K. Liu, L. X. Yang, Y. Sun, T. Zhang, H. Peng, H. F. Yang, C. Chen, Y. Zhang, Y. F. Guo, D. Prabhakaran, M. Schmidt, Z. Hussain, S. K. Mo, C. Felser, B. Yan, and Y. L. Chen, *Nat. Mater.* **15**, 27 (2016).
- [15] K. Kuroda, T. Tomita, M. T. Suzuki, C. Bareille, A. A. Nugroho, P. Goswami, M. Ochi, M. Ikhlas, M. Nakayama, S. Akebi, R. Noguchi, R. Ishii, N. Inami, K. Ono, H. Kumigashira, A. Varykhalov, T. Muro, T. Koretsune, R. Arita, S. Shin, T. Kondo, and S. Nakatsuji, *Nat. Mater.* **16**, 1090 (2017).
- [16] E. Liu, Y. Sun, N. Kumar, L. Muechler, A. Sun, L. Jiao, S. Y. Yang, D. Liu, A. Liang, Q. Xu, J. Kroder, V. Süß, H. Borrmann, C. Shekhar, Z. Wang, C. Xi, W. Wang, W. Schnelle, S. Wirth, Y. Chen, S. T. B. Goennenwein, and C. Felser, *Nat. Phys.* **14**, 1125 (2018).
- [17] A. A. Soluyanov, D. Gresch, Z. Wang, Q. Wu, M. Troyer, X. Dai, and B. A. Bernevig, *Nature* **527**, 495 (2015).
- [18] A. A. Zyuzin and R. P. Tiwari, *JETP Lett.* **103**, 717 (2016).
- [19] Y. Wu, D. Mou, N. H. Jo, K. Sun, L. Huang, S. L. Bud'ko, P. C. Canfield, and A. Kaminski, *Phys. Rev. B* **94**, 121113(R) (2016).
- [20] K. Deng, G. Wan, P. Deng, K. Zhang, S. Ding, E. Wang, M. Yan, H. Huang, H. Zhang, Z. Xu, J. Denlinger, A. Fedorov, H. Yang, W. Duan, H. Yao, Y. Wu, S. Fan, H. Zhang, X. Chen, and S. Zhou, *Nat. Phys.* **12**, 1105 (2016).
- [21] Z. Wang, D. Gresch, A. A. Soluyanov, W. Xie, S. Kushwaha, X. Dai, M. Troyer, R. J. Cava, and B. A. Bernevig, *Phys. Rev. Lett.* **117**, 056805 (2016).
- [22] A. Tamai, Q. S. Wu, I. Cucchi, F. Y. Bruno, S. Riccò, T. K. Kim, M. Hoesch, C. Barreteau, E. Giannini, and C. Besnard, *Phys. Rev. X* **6**, 31021 (2016).
- [23] I. Belopolski, P. Yu, D. S. Sanchez, Y. Ishida, T. R. Chang, S. S. Zhang, S. Y. Xu, H. Zheng, G. Chang, G. Bian, H. T. Jeng, T. Kondo, H. Lin, Z. Liu, S. Shin, and M. Z. Hasan, *Nat. Commun.* **8**, 942 (2017).
- [24] E. Haubold, K. Koepf, D. Efremov, S. Khim, A. Fedorov, Y. Kushnirenko, J. Van Den Brink, S. Wurmehl, B. Büchner, T. K. Kim, M. Hoesch, K. Sumida, K. Taguchi, T. Yoshikawa, A. Kimura, T. Okuda, and S. V. Borisenko, *Phys. Rev. B* **95**, 241108(R) (2017).
- [25] H. Zheng, H. Lin, T. Neupert, Y. Bian, M.-A. Hsuan, C.-H. Hsu, H. Lu, I. Belopolski, A. Bansil, G. Chang, M. Z. Hasan, D. S. Sanchez, X. Zhang, N. Alidoust, B. Singh, S. Jia, V. N. Strocov, S.-Y. Xu, G. Bian, S.-M. Huang, H.-T. Jeng, and T.-R. Chang, *Sci. Adv.* **3**, e1603266 (2017).

- [26] S. Borisenko, D. Evtushinsky, Q. Gibson, A. Yaresko, T. Kim, M. N. Ali, B. Buechner, M. Hoesch, and R. J. Cava, ArXiv Prepr. ArXiv1507.04847 (2015).
- [27] D. Chaudhuri, B. Cheng, A. Yaresko, Q. D. Gibson, R. J. Cava, and N. P. Armitage, Phys. Rev. B **96**, 075151 (2017).
- [28] G. Chang, B. Singh, S. Y. Xu, G. Bian, S. M. Huang, C. H. Hsu, I. Belopolski, N. Alidoust, D. S. Sanchez, H. Zheng, H. Lu, X. Zhang, Y. Bian, T. R. Chang, H. T. Jeng, A. Bansil, H. Hsu, S. Jia, T. Neupert, H. Lin, and M. Z. Hasan, Phys. Rev. B **97**, 041104(R) (2018).
- [29] L. A. Kuznetsova, V. L. Kuznetsov, and D. M. Rowe, J. Phys. Chem. Solids **61**, 1269 (2000).
- [30] S. Kuypers, G. Van Tendeloo, J. Van Landuyt, and S. Amelinckx, Micron Microsc. Acta **18**, 245 (2002).
- [31] D. S. Lee, T. H. Kim, C. H. Park, C. Y. Chung, Y. S. Lim, W. S. Seo, and H. H. Park, CrystEngComm **15**, 5532 (2013).
- [32] A. M. Essin and V. Gurarie, Phys. Rev. B **85**, 195116 (2012).
- [33] M. M. Otrokov, I. P. Rusinov, M. Blanco-Rey, M. Hoffmann, A. Y. Vyazovskaya, S. V. Eremeev, A. Ernst, P. M. Echenique, A. Arnau, and E. V. Chulkov, Phys. Rev. Lett. **122**, 107202 (2019).
- [34] D. Zhang, M. Shi, T. Zhu, D. Xing, H. Zhang, and J. Wang, ArXiv Prepr. ArXiv1808.08014 (2018).
- [35] M. M. Otrokov, I. I. Klimovskikh, H. Bentmann, A. Zeugner, Z. S. Aliev, S. Gass, A. U. B. Wolter, A. V. Koroleva, D. Estyunin, and A. M. Shikin, ArXiv Prepr. ArXiv1809.07389 (2018).
- [36] Y. Gong, J. Guo, J. Li, K. Zhu, M. Liao, X. Liu, Q. Zhang, L. Gu, L. Tang, and X. Feng, ArXiv Prepr. ArXiv1809.07926 (2018).
- [37] B. Chen, F. Fei, D. Zhang, B. Zhang, W. Liu, S. Zhang, P. Wang, B. Wei, Y. Zhang, and J. Guo, ArXiv Prepr. ArXiv1903.09934 (2019).
- [38] S. V. Eremeev, M. M. Otrokov, and E. V. Chulkov, J. Alloys Compd. **709**, 172 (2017).
- [39] See Supplemental Material at [URL will be inserted by publisher] for more details on analyses for XRD and PND data, theoretical calculations, and specific heat measurements.
- [40] G. Kresse and J. Furthmüller, Phys. Rev. B **54**, 11169 (1996).
- [41] G. Kresse and J. Furthmüller, Comput. Mater. Sci. **6**, 15 (1996).
- [42] V. Petříček, M. Dušek, and L. Palatinus, Zeitschrift Für Krist. Mater. **229**, 345 (2014).
- [43] J. Rodríguez-Carvajal, CEA/Saclay, Fr. (2001).
- [44] Q. Zhang, T. Heitmann, Z. L. Huang, W. D. Wu, D. Vaknin, B. C. Sales, R. J. McQueeney, and I. Mnb, ArXiv Prepr. ArXiv1902.10110 (2019).
- [45] E. J. J. Mallmann, A. S. B. Sombra, J. C. Goes, and P. B. A. Fechine, Solid State Phenom. **202**, 65 (2013).
- [46] M. M. Otrokov, I. I. Klimovskikh, H. Bentmann, A. Zeugner, Z. S. Aliev, S. Gass, A. U. B. Wolter, A. V. Koroleva, D. Estyunin, A. M. Shikin, M. Blanco-Rey, M. Hoffmann, A. Y.

- Vyazovskaya, S. V. Ereemeev, Y. M. Koroteev, I. R. Amiraslanov, M. B. Babanly, N. T. Mamedov, N. A. Abdullayev, V. N. Zverev, B. Büchner, E. F. Schwier, S. Kumar, A. Kimura, L. Petaccia, G. Di Santo, R. C. Vidal, S. Schatz, K. Kißner, C.-H. Min, S. K. Moser, T. R. F. Peixoto, F. Reinert, A. Ernst, P. M. Echenique, A. Isaeva, and E. V. Chulkov, *ArXiv Prepr. ArXiv1809.07389* (2018).
- [47] B. A. Kuropatwa and H. Kleinke, *Zeitschrift Fur Anorg. Und Allg. Chemie* **638**, 2640 (2012).
- [48] A. Zeugner, F. Nietschke, A. U. B. Wolter, S. Gaß, R. C. Vidal, T. R. F. Peixoto, D. Pohl, C. Damm, A. Lubk, R. Hentrich, S. K. Moser, C. Fornari, C. H. Min, S. Schatz, K. Kißner, M. Ünzelmann, M. Kaiser, F. Scaravaggi, B. Rellinghaus, K. Nielsch, C. Hess, B. Büchner, F. Reinert, H. Bentmann, O. Oeckler, T. Doert, M. Ruck, and A. Isaeva, *Chem. Mater.* **31**, 2795 (2019).

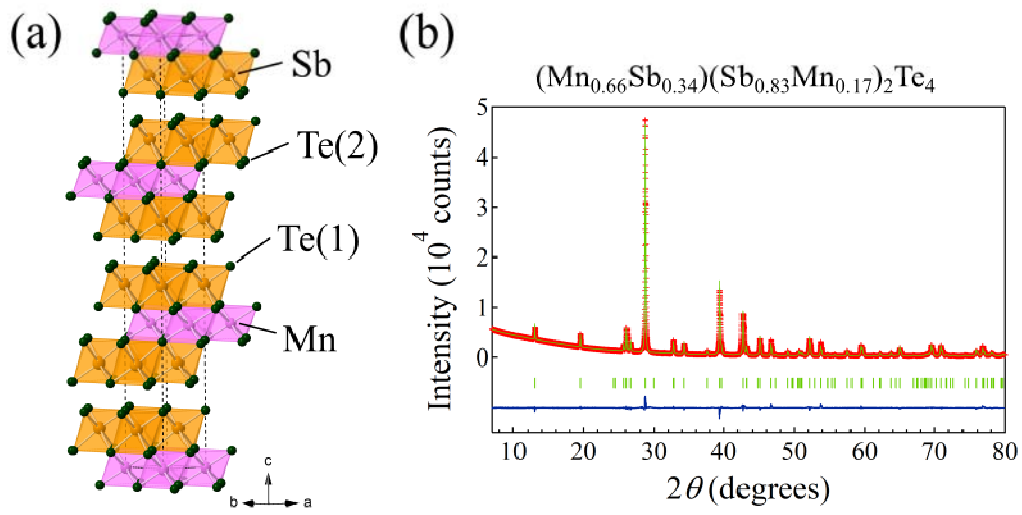


FIG. 1. (a) Crystal structure of MnSb_2Te_4 . Pink, orange, and dark blue sphere represent Mn, Sb, Te, respectively. Note that there is several amount of anti-site disorders between Sb and Mn sites. (b) Observed and calculated XRD patterns of MnSb_2Te_4 . Red crosses, green and blue lines represent observed, calculated, and difference profiles. Green ticks are used to show the positions of the Bragg peaks.

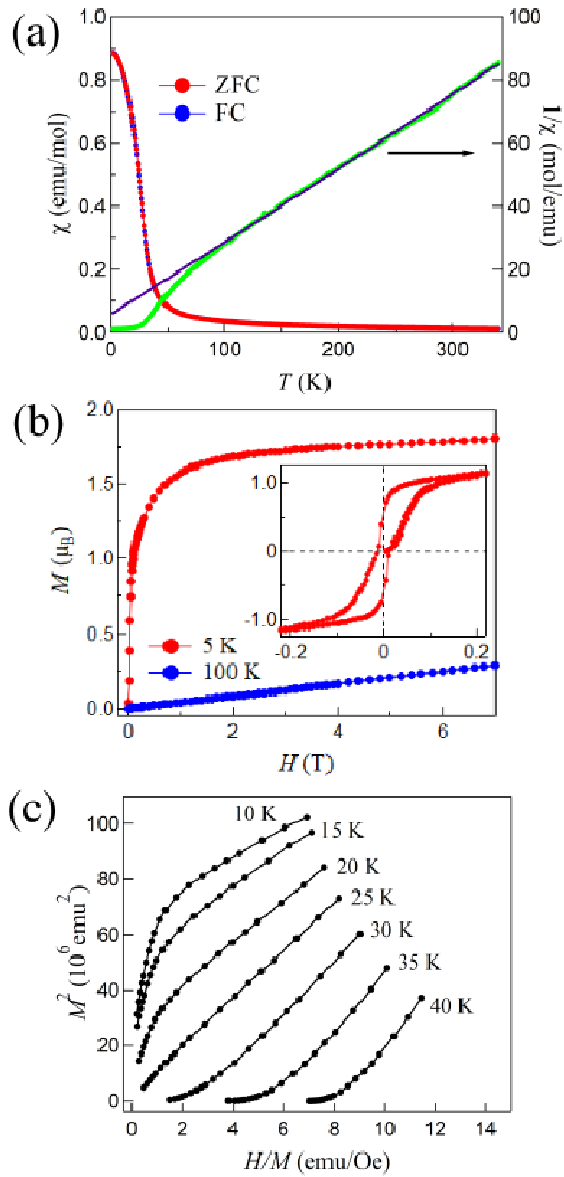


FIG. 2. (a) (left) Temperature dependence of magnetic susceptibility under an applied field of 0.1 T with zero-field cooling (red) and field cooling (blue) process. (right) Temperature dependence of inverse susceptibility. (b) Isothermal magnetization curves at 5 K (red) and 100 K (blue). The inset shows a hysteresis loop. (c) M^2 versus H/M (Arrott plot) at various temperatures around T_C .

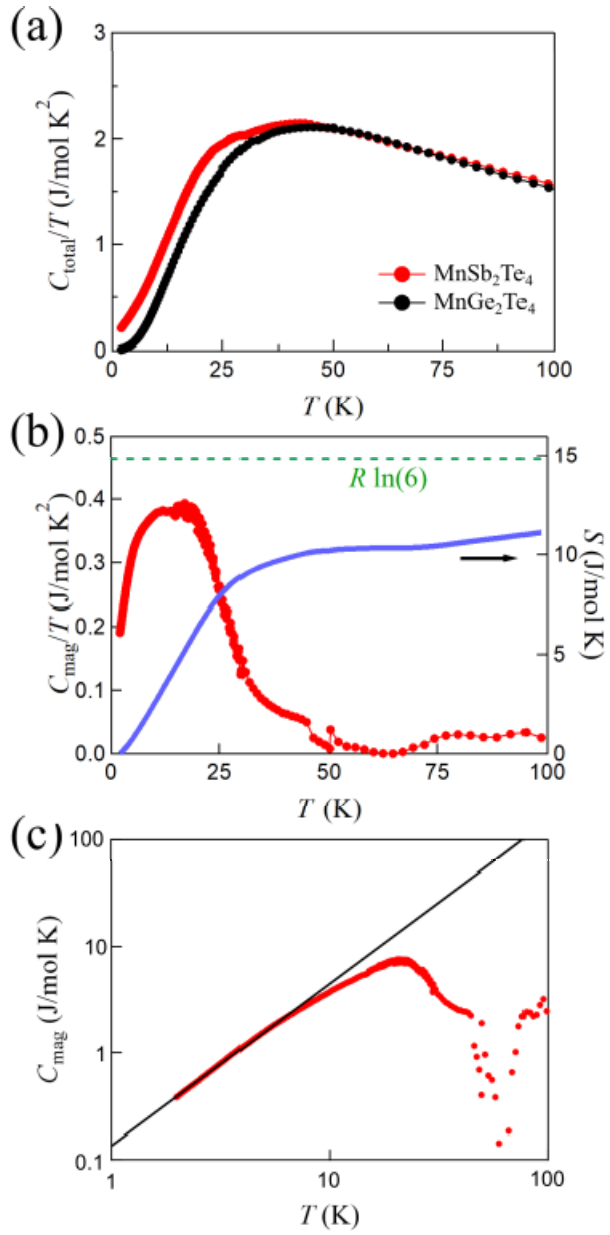


FIG. 3. (a) (left) The magnetic part of the specific heat divided by temperature. (right) the magnetic entropy. The horizontal line indicates $R \ln 6$ (c) The magnetic part of the specific heat in full logarithmic scale.

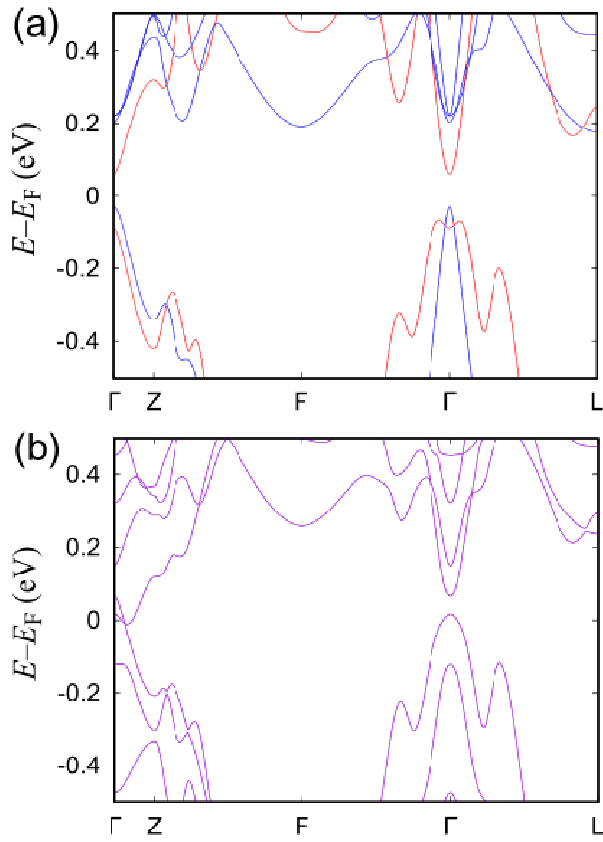


FIG. 4. Calculated band structures for MnSb₂Te₄ (a) without and (b) with SOC. In (a), the red (blue) color represents up-spin (down-spin) bands.

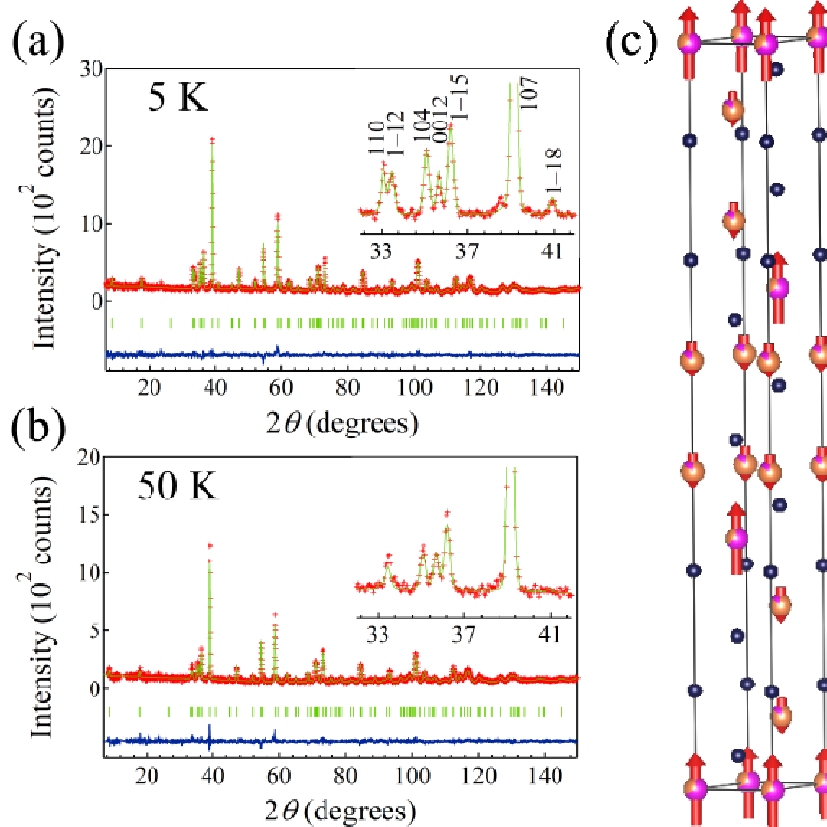


FIG. 5. PND patterns of MnSb_2Te_4 at (a) 5 K and (b) 50 K. Red crosses, green and blue lines represent observed, calculated, and difference profiles. Green ticks are used to show the positions of the Bragg peaks. (c) Proposed magnetic structure obtained from 5 K data.

TABLE I. Crystallographic data for MnSb_2Te_4 obtained from XRD at room temperature (upper) and PND at 50 K (lower) data. Assumed space group is $R\bar{3}m$ with $a = 4.2385(3) \text{ \AA}$, $c = 40.8497(3) \text{ \AA}$ from XRD, and $a = 4.2219(2) \text{ \AA}$, $c = 40.606(3) \text{ \AA}$ from PND. g represents the occupancy factor of each site, and U_{iso} employs an overall Debye-Waller factor.

| Atom | Site | g^b | x | y | z | $U_{iso}/100 \text{ \AA}^2$ |
|------|------|-----------|-----|-----|--------------|-----------------------------|
| Mn1 | 3a | 0.6645(3) | 0 | 0 | 0 | 1.62(3) |
| | | 0.666(7) | | | | 0.6(1) |
| Sb1 | 3a | 0.3355(3) | 0 | 0 | 0 | 1.62(3) |
| | | 0.333(7) | | | | 0.6(1) |
| Sb2 | 6c | 0.8323(3) | 0 | 0 | 0.42802(15) | 1.62(3) |
| | | 0.833(4) | | | 0.4254(2) | 0.6(1) |
| Mn2 | 6c | 0.1677(3) | 0 | 0 | 0.424802(15) | 1.62(3) |
| | | 0.167(4) | | | 0.4254(2) | 0.6(1) |
| Te1 | 6c | 1 | 0 | 0 | 0.131456(12) | 1.06(3) |
| | | | | | 0.13160(11) | 0.6(1) |
| Te2 | 6c | 1 | 0 | 0 | 0.292259(14) | 1.29(3) |
| | | | | | 0.29175(13) | 0.6(1) |